Polarized coherent microwave supercontinua with a terawatt laser driver

A. V. Mitrofanov,[1,2,3,4] A. A. Voronin,[1,2,5] M. M. Nazarov [ORCID],[3] M. V. Rozhko,[1,2] P. A. Shcheglov,[3] M. V. Chashchin [ORCID],[1,3]
P. B. Glek,[1] A. B. Fedotov,[1,2,5] D. A. Sidorov-Biryukov,[1,2,3,5] V. Ya. Panchenko,[1,3,4] and A. M. Zheltikov[1,2,5,6,*]

[1]*Physics Department, M.V. Lomonosov Moscow State University, Moscow 119992, Russia*
[2]*Russian Quantum Center, Skolkovo, Moscow Region 143025, Russia*
[3]*Kurchatov Institute National Research Center, Moscow 123182, Russia*
[4]*Inst. Laser and Information Technol. - Branch of FSRC "Crystallography and Photonics," Russian Acad. Sci., Shatura 140700, Russia*
[5]*Kazan Quantum Center, A.N. Tupolev Kazan National Research Technical University, 420126 Kazan, Russia*
[6]*Department of Physics and Astronomy, Texas A&M University, College Station, Texas 77843, USA*

Ultrafast laser-plasma interactions driven by ultrashort terawatt laser pulses are shown to give rise to a bright multioctave microwave radiation, whose polarization and spatial mode structure provides a sensitive probe for laser-driven plasma electrodynamics, helping detect the symmetries of plasma currents and signatures of multiple ionization. Polarization mode structure of this radiation is dominated, as polarization-resolved measurements show, by a radially polarized mode, indicating the significance of ponderomotively driven plasma currents as sources of microwave emission. Angle-resolved analysis of microwave supercontinua reveals regimes in which the microwave emission is drastically enhanced, via coherence buildup, manifested in a well-resolved Cherenkov-emission cone.

I. INTRODUCTION

Generation of terahertz (THz) radiation by ultrashort high peak-power laser pulses [1–3] is one of the central effects in contemporary ultrafast laser-plasma physics. Lying on the borderline between ultrafast nonlinear optics and strong-field science, this effect helps understand complex laser-plasma dynamics [4–9] and brings the promise of bright THz sources for medical imaging, safety screening, communication technologies, and material characterization [10]. If extended to even higher-power laser settings and toward lower, sub-THz and microwave (μWv) frequencies [11–19], laser-plasma sources of low-frequency secondary radiation could help advance fundamental laser research and cutting-edge photonic technologies by enabling creation of bright microwave sources for astrophysical research and remote sensing, providing means to explore new regimes of laser-matter interactions [5–9,20], and opening new avenues in high-speed optoelectronics [21–23], laser-plasma particle acceleration [24], optical spintronics [25], and laser valleytronics [26,27].

Such an extension, however, faces serious difficulties related to multifilamentation instabilities of high-power laser beams, field-intensity clamping due to plasma refraction, and low-frequency cutoff of plasma dispersion. Overcoming or working around these limitations is only possible through a deeper understanding of the physics behind THz and microwave generation in laser plasmas. While THz radiation by laser filaments and plasmas induced by a two-color laser driver can usually be adequately understood in terms of trans-

verse photoionization currents [3,8,18,28–30], the physics behind THz generation in laser-plasma experiments with a single-color laser driver is still open to debate. As a significant milestone, Sprangle *et al.* [5] and Thiele *et al.* [6] have developed a model of THz generation by longitudinal plasma currents driven with laser-induced pondermotive forces inside laser filaments, providing an adequate explanation for many of the properties of THz radiation in single-color-laser-filament experiments [4,7,31]. Defining the agenda for the present-day research in this area are the questions as to whether or not this THz generation scenario can be extended toward lower output frequencies, enabling efficient microwave generation, and whether or not this scenario can be scaled to higher driver and THz output powers.

Here, we aim to address these questions via an accurate polarization-, pressure-, and emission-angle-resolved analysis of broadband microwave radiation emitted by gas plasmas induced by ultrashort terawatt (TW) laser pulses. Setting the scene for such a study are the results of the latest experiments [16,19,32], revealing a nonmonotonic behavior of the THz/sub-THz output of laser filaments and laser plasmas as a function of the gas pressure and the emission angle, suggesting that a well-defined emission cone may be showing up in laser–plasma interaction regimes where THz/sub-THz generation is especially efficient. Experiments presented below in this paper demonstrate that, with a suitable gas pressure adjustment, such laser-plasma schemes of low-frequency radiation generation can be extended to higher, terawatt-level laser powers and toward lower, microwave radiation frequencies. As an expansion of the existing toolbox for THz/sub-THz/μWv field characterization, we present careful polarization-resolved studies cross-referenced against

*zheltikov@physics.msu.ru

polarization analysis of microwave radiation generated in two-color laser-plasma experiments.

In experiments with a single-color laser driver, the polarization mode structure of microwave radiation is shown to be dominated by a radially polarized mode, indicating the dominant role of ponderomotively driven longitudinal plasma currents as sources of microwave emission. This polarization mode structure is in a stark contrast with linearly polarized microwave radiation generated by transverse plasma currents, playing the predominant role in low-frequency radiation emission in two-color laser-plasma experiments. In agreement with earlier studies [16], our angle-resolved analysis of microwave supercontinua reveals a conical emission pattern of microwave radiation. We extend this analysis by comparing the experimental emission patterns to the Cherenkov-cone patterns, as dictated by the canonical Frank-Tamm solution [33,34] for the fields radiated by a longitudinal electric current. This analysis shows that the Cherenkov emission cone provides a close fit for the angular profiles of microwave radi-

ation in laser-plasma experiments, offering important insights into the physics behind the coherent buildup of the microwave output in laser plasma experiments and suggesting the ways toward laser-plasma sources of bright microwave radiation.

II. THEORETICAL FRAMEWORK

A. The physical model

In search for a laser-plasma interaction setting that would best suit the purpose of bright multiband, microwave-THz radiation generation by TW and multi-TW laser pulses, we resort to the equations for the radiation of photoionization and ponderomotively driven plasma currents, as derived by Sprangle *et al.* [5] and Thiele *et al.* [6], and explore the means of enhancing the lowest-frequency output of plasma-current emission within the experimentally accessible parameter landscape. As a part of this search, we numerically solve a standard nonlinear evolution equation for an ultrashort laser pulse in a fast-ionizing gas [35,36],

$$
\begin{aligned}
\frac{\partial}{\partial z}A(r,z,\omega) = {} & \left[\frac{ic}{2\omega n_0}\Delta_\perp + iD(\omega)\right]A(r,z,\omega) + i\frac{\omega\, n_{2e}}{c}F^{-1}[I(r,z,\eta)] \\
& - \left[\frac{ie^2\omega}{2cn_0 m\varepsilon_0\left(\omega^2 + \tau_e^{-2}\right)} + \frac{\sigma(\omega)}{2}\right]F[\rho(r,z,\eta)A(r,z,\eta)] \\
& - F\left[\frac{\sum_{i=1}^{10}U_i(r,z,\eta)w_i(r,z,\eta)\rho_{i-1}(r,z,\eta)}{2I(r,z,\eta)}A(r,z,\eta)\right],
\end{aligned}
\tag{1}
$$

where $A(r,z,\eta)$ is the field envelope, $A(r,z,\omega)$ is its Fourier transform, $I(r,z,\eta) = |A(r,z,\eta)|^2$ is the field intensity, r is the transverse coordinate, z is the coordinate along the propagation axis, η is the retarded time, $\omega = 2\pi c/\lambda$ is the radiation frequency, λ is the wavelength, c is the speed of light in vacuum, F and F^{-1} are, respectively, the forward and backward Fourier transform operators, $\Delta_\perp$ is the transverse Laplace operator, $D = k(\omega) - \omega/\upsilon_g$, υ_g is the group velocity, n_{2e} is the electronic part of the nonlinear refractive index, $k(\omega) = \omega n(\omega)/c$, $n(\omega)$ is the refractive index, $U_i = U_i^0 + U_{osc}$, U_i^0 is the ith ionization potential, U_{osc} is the energy of field-induced electron oscillations, w_i is the rate of ith ionization, $\sigma(\omega) = e^2\tau_e[m\varepsilon_0 n_0 c(1 + \omega^2\tau_e^2)]^{-1}$ is the impact-ionization cross section, τ_e is the collision time, and e and m are the electron charge and mass, respectively.

Ionization dynamics is included via a set of coupled equations for the electron density ρ and the densities ρ_i of multiply charged ions:

$$d\rho_0(t)/dt = -w_1(t)\rho_0(t),$$

$$d\rho_i(t)/dt = w_i(t)\rho_{i-1}(t) - w_{i+1}(t)\rho_i(t) \text{ for } i \text{ from 1 to 9,}$$

$$d\rho_{10}(t)/dt = w_{10}(t)\rho_9(t),$$

$$\rho = \sum_{i=1}^{10} i\rho_i, \tag{2}$$

where ρ_0 is the density of neutral species and ρ_i is the density of multiply charged ions with an ionization multiplicity i.

Simulations were performed using graphic-processor unit laboratory clusters [37,38], as well as a shared

research facility of high-performance supercomputing resources at M.V. Lomonosov Moscow State University. In Figs. 1(a)–1(h), we present the results of numerical modeling performed for a laser driver with a central wavelength $\lambda_0 = 0.8\,\mu m$, pulse width $\tau_0 = 35$ fs, an input beam diameter $d_0 = 6$ cm, and a pulse energy E_0 up to 100 mJ—a set of parameters typical of the short-pulse output of a Ti: sapphire (TiS) laser used in experiments presented below. This laser driver is focused into a gas cell filled with molecular nitrogen, argon, or atmospheric air at a variable gas pressure p. Dispersion of these gases is included in the model through a suitable Sellmeier equation [39,40]. The electronic nonlinearity is calculated via the nonlinear refractive index $n_{2e} = n_{20}(p/p_0)$, with $p_0 = 1$ bar, $n_{20} \approx 1.5 \times 10^{-19}$ cm^2/W for Ar [35,41], leading to a critical power of self-focusing, $P_{cr} \approx 6.3$ GW at $p = 1$ atm. The ionization rates $w_i(I)$ are calculated by using the Keldysh formalism [42]. The ith-ionization potentials for argon are taken, in accordance with Ref. [43], as $U_1^0 = 15.8$ eV, $U_2^0 = 27.6$ eV, $U_3^0 = 40.7$ eV, $U_4^0 = 59.6$ eV, $U_5^0 = 74.8$ eV, $U_6^0 = 91.3$ eV, $U_7^0 = 124$ eV, $U_8^0 = 143$ eV, $U_9^0 = 422$ eV, and $U_{10}^0 = 480$ eV. The collision time τ_e is set at $\tau_e = 200(p_0/p)$ fs [41].

B. Field evolution and ultrafast ionization dynamics

Ultrafast ionization of the gas by the focused laser driver, whose intensity increases toward the beam waist [Figs. 1(a), 1(c), 1(e), and 1(f)], gives rise to a rapid buildup of the electron density $\rho(r,z,\eta)$ [Figs. 1(b), 1(d), and 1(g)],
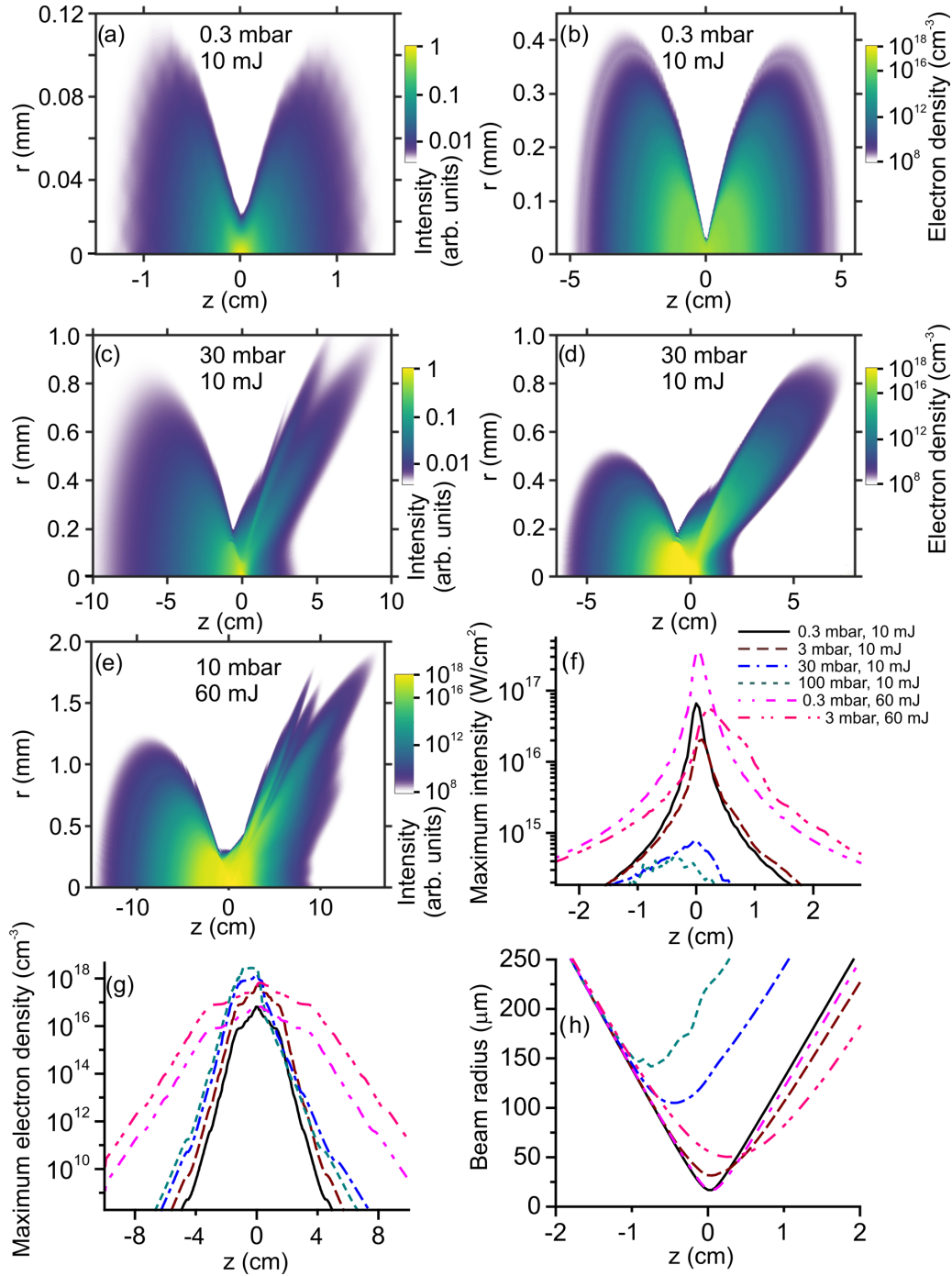
FIG. 1. Nonlinear dynamics of a terawatt laser pulse with a central wavelength $\lambda_0 = 0.8\,\mu$m, a pulse width $\tau_0 = 35$ fs, and an input beam diameter $d_0 = 7$ cm focused, with a focal length $f = 2.5$ m, into a gas cell filled with argon at a variable gas pressure p: (a)–(e) rz maps of the field intensity integrated over the pulse $\int_{-\infty}^{\infty} I_L(r, z, \eta)d\eta$ (a), (c), (e) and the electron density in the wake of the laser pulse (b), (d), (f) maximum field intensity $\max_{r,\eta} I_L(r, z, \eta)$, (g) maximum electron density $\max_{r,\eta} \rho(r, z, \eta)$, and (h) beam-radius trajectory $r_L(z)$. The pulse energies and gas pressures are as specified in the panels.

translating into a transverse profile of the refractive index $\delta n_p(r, z, \eta) \approx -[\omega_p(r, z, \eta)]^2/(2\omega_0^2)$, where $\omega_p(r, z, \eta) = [4\pi e^2 \rho(r, z, \eta)/m]^{1/2}$ is the plasma frequency, e and m are the electron charge and electron mass, r and z are the radial and longitudinal coordinates, and η is the retarded time, i.e., the time in the frame of reference that copropagates with the driver pulse. At low p and E_0 [$p = 0.3$ mbar and $E_0 = 10$ mJ in Figs. 1(a) and 1(b)], the Kerr and ionization nonlinearities

are weak. The space-time dynamics of the laser field remains linear in this regime over the entire beam path [Fig. 1(a)]. The respective map of the electron density is almost symmetric [Fig. 1(b)] relative to the beam focus at $z = 0$.

At higher p and E_0, the transverse profile of the refractive index $\delta n_p(r, z, \eta)$ leads to a refraction of the laser beam, which makes the geometry of beam focusing deviate from linear, $\delta n_p = 0$ beam caustic [Figs. 1(c),
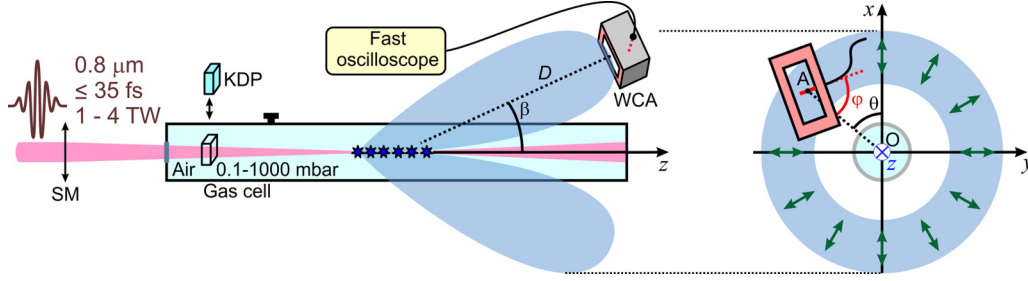
FIG. 2. Experimental setup: SM, spherical mirror; KDP, crystal for second-harmonic generation, WCA, waveguide-to-coaxial adapter. Also shown are the radially polarized mode of THz/μWv radiation (green arrows), detection angle β, the angle θ between the x axis and direction to the WCA in the xy plane (the OA line), the angle φ between the coaxial cable of the WCA (shown red) and the OA line.

1(e), and 1(f)]. To gain insights into this nonlinear beam dynamics, we examine the z dependence of the effective beam radius of the laser driver, defined as $r_L(z) = [\int_0^\infty F(r, z) 2\pi r^3 dr]^{1/2} / [\int_0^\infty F(r, z) 2\pi r dr]^{1/2}$, where $F(r, z) = \int_{-\infty}^\infty I_L(r, z, \eta) dt$, where $I_L(r, z, \eta)$ is the laser intensity. As a meaningful reference, the solid line in Fig. 1(h) shows the $r_L(z)$ trajectory that represents a linear beam caustic, i.e., the geometry of beam focusing with the same f, but with $p = 0$, or, equivalently, $\delta n_p = 0$. As long as the electron density $\rho(r, z, \eta)$ remains low, plasma refraction $\delta n_p(r, z, \eta)$ continues to build up along z toward the beam focus at $z = z_f$, eventually arresting the growth of the driver intensity [Fig. 1(f)] and limiting the electron density [Fig. 1(g)].

Analysis of the maps of space-time field evolution, presented in Fig. 1 side by side with the maps of the electron density is in many ways instructive as it reveals clear signatures of multiple ionization. As single ionization is depleted by a high-intensity laser field; the buildup of $\delta n_p(r, z, \tau_0)$ is no longer there to limit the growth of field intensity in a laser beam, which thus continues self-focusing until multiple ionization kicks in [44], to prevent the beam from collapsing and keep the growth of $I_L(r, z, \eta)$ in check [Figs. 1(c)–1(g)].

With insights from the generic equation for the ponderomotive source term behind secondary radiation by plasma currents [5,6], the essential pressure-dependent factors in laser-plasma emission are conveniently grouped into $\mathcal{R}(p) = \rho I_L / (\nu_e \tau_0)$, with the electron collision rate ν_e defining the $\omega \approx \nu_e$ low-frequency cutoff of plasma-current emission. Combined with a monotonic increase of ν_e as a function of p, a monotonically decreasing $I_L(p)$ [Fig. 1(f)] translates, via $\mathcal{R}(p)$ and despite a slow growth of $\rho(p)$ [Fig. 1(g)], into a monotonic decrease of the microwave-THz yield with the growth in p in a broad range of gas pressures. At low p and low P_0, however, the space-time dynamics of the laser field is linear [Fig. 1(a)], leading the microwave-THz yield to deviate from a uniformly monotonic behavior as a function of the gas pressure, precisely as observed in experiments presented below.

III. EXPERIMENT

Providing a high-P_0 driver for μWv-THz generation in our studies (Fig. 2) is an amplified output of a TiS laser [45,46], delivering near-IR pulses with $\lambda_0 \approx 0.8 \ \mu$m, τ_0 of ≈ 25–35 fs, and a pulse energy up to ≈ 100 mJ, translating into peak powers up to $P_0 \approx 4$ TW. The TiS-laser output is focused into

a gas cell with a large-aperture, 2.5-m focal-length spherical mirror (Fig. 2). The gas pressure p inside the cell is varied from 0.1 mbar to 1.0 bar. In experiments with a two-color laser driver, an in-house grown <150-μm-thick potassium dihydrogen phosphate (KDP) crystal (Fig. 2) is placed right behind the gas-cell entrance window to generate the second driver field, at the frequency of the second harmonic (SH), $2\omega_0 = \pi c / \lambda_0$, with a typical efficiency of about 5%.

When focused into the gas cell, a single-color (0.8-μm only) or two-color (the 0.8-μm TiS-laser output and its SH) driver gives rise to broadband, supercontinuum radiation, whose spectrum covers most of the THz range and stretches deep into the microwave region. The microwave part of this supercontinuum is detected (Fig. 2) using three waveguide-to-coaxial adapters (WCAs), providing detection ranges from ≈ 2 to 12 GHz (WCA1), ≈ 4 to 18 GHz (WCA2), and ≈ 12 to 32 GHz (WCA3). The WCA output is analyzed and recorded with a 20-GHz oscilloscope (Fig. 2). The spatial mode properties of μWv radiation are studied by scanning the WCA detector in the angle β between the z axis and the direction to the WCA (Fig. 2). Polarization of microwave radiation is analyzed by measuring the microwave output as a function of the angle θ between the x axis and direction to the WCA in the xy plane (the OA line in Fig. 2) and the angle φ between the coaxial cable of the WCA (shown red in Fig. 2) and the OA line (Fig. 2).

IV. RESULTS AND DISCUSSION

A. Time-resolved analysis

In Fig. 3(a), we present a typical temporal trace of μWv radiation detected with WCA2 in an experiment with a single-color driver with $\lambda_0 \approx 0.8 \ \mu$m, $\tau_0 \approx 35$ fs, $E_0 \approx 60$ mJ, and $d_0 \approx 7$ cm, focused into a gas cell filled with air at $p \approx 0.5$ mbar. The field intensity in such a laser beam is estimated at ≈ 50 GW/cm^2. The field intensity in a focused laser beam in this experiment, as both measurements and simulations show [Fig. 1(f)], may reach the level of 3×10^{17} W/cm^2 on the axis of the plasma channel. While this level of laser intensity is high enough to induce M-electron ionization with large M, only single ionization plays a noticeable role in microwave generation in our experiments, as microwave radiation is confined to the outer, off-axis plasma layers, where the laser field intensity is much weaker, while low-ω radiation generated in the central plasma regions, where the field intensity is high, is screened by the plasma, never making it to the space outside
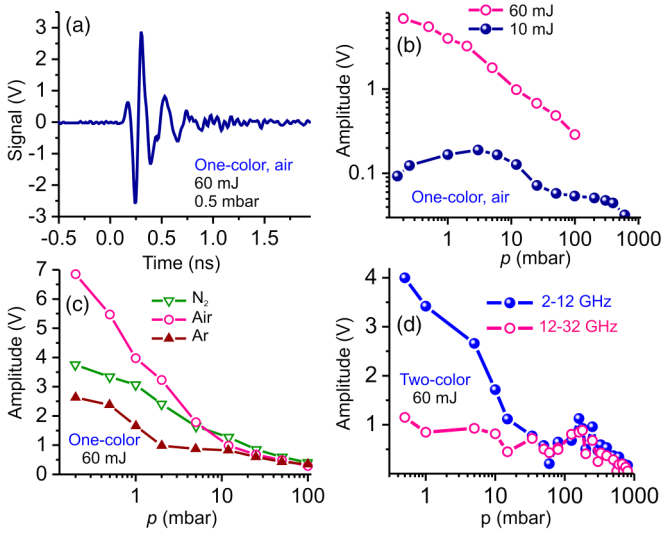
FIG. 3. (a) Temporal trace of microwave radiation detected with WCA2 in an experiment with a single-color driver with $\lambda_0 \approx 0.8\,\mu$m, $\tau_0 \approx 35$ fs, and $E_0 \approx 60$ mJ focused into a gas cell filled with air at $p \approx 0.5$ mbar. (b) Pressure scans of the microwave output of laser plasmas driven in air by laser pulses with $\lambda_0 \approx 0.8\,\mu$m, $\tau_0 \approx 35$ fs, and $E_0 \approx 10$ mJ (blue filled circles) and 60 mJ (pink open circles). (c), (d) Pressure scans of the microwave output of laser plasmas driven by a single-color (c) and two-color (d) laser field with $\lambda_0 \approx 0.8\,\mu$m, $\tau_0 \approx 35$ fs, and $E_0 \approx 60$ mJ in (c) N_2 (open green triangles), air (open pink circles), and argon (filled wine triangles) and (d) atmospheric air. Measurements are performed using WCAs with detection ranges of (c) 4 to 18 GHz and (d) 2 to 12 GHz (blue line) and 12 to 32 GHz (pink line).

FIG. 4. (a) The microwave output Φ of laser plasmas driven by a two-color laser field in air at $p \approx 0.5$ mbar vs the pulse energy E_0 of the laser driver with $\lambda_0 \approx 0.8\,\mu$m, $\tau_0 \approx 35$ fs, and the peak power P_0 as shown in the upper axis. Measurements are within the WCA detection range of 2 to 12 GHz (blue) and 12 to 32 GHz (pink). (b) The microwave output measured as a function of β with WCA1 (blue) and WCA2 (red) at $D \approx 40$ cm for $\lambda_0 \approx 0.8\,\mu$m, $\tau_0 \approx 35$ fs, $E_0 \approx 60$ mJ, and $p \approx 3$ mbar: (circles) experimental results and (dashed line) their best fit with the Cherenkov phase-matching function $\Im(\beta)$. (c), (d) Polarization-resolved microwave output as a function of the angle θ measured in a single-color (c) and two-color (d) experiment with $\lambda_0 \approx 0.8\,\mu$m, $\tau_0 \approx 35$ fs, $E_0 \approx 60$ mJ, $E_{\rm SH} \approx 2.5$ mJ, and $p \approx 1$ mbar (c) and 50 mbar (d) with WCA2 at $D \approx 40$ cm and $\varphi \approx 0°$ (filled blue circles) and $\varphi \approx 90°$ (open pink circles). The solid line is the best $\xi \cos(\theta - \alpha)$ fit, with (c) $\xi = 0$ and (d) $\xi = 1$, $\alpha = 70°$ (blue line) and $\xi = 0.5$, $\alpha = 160°$ (pink line).

the plasma channel. The maximum peak power of laser pulses in these experiments ($P_0 \approx 1.7$ TW for laser pulses with $E_0 \approx 60$ mJ and $\tau_0 \approx 35$ fs) is more than an order of magnitude lower than the level of laser peak powers ($P_r \approx 30$ TW for $\rho \approx 10^{18}$ cm^{-3}) where effects of relativistic self-focusing and channeling [47,48] start to play a role.

With a typical 2–12-GHz microwave readout in our experiments yielding a peak voltage above 4.0 V [Fig. 4(a)] across a 50-Ω input resistance and with an emission pulse width of $\approx$200 ps, a WCA-to-oscilloscope signal conversion efficiency of $\approx$10%, the total energy of microwave radiation emitted within $\Delta\beta_{\rm GHz} \approx 20°$ in our experimental setting is estimated at 1.4 μJ, corresponding to a microwave peak power of about 7 kW.

B. Pressure scans

Spectral studies were performed within a broad range of p and P_0, with the low-frequency secondary radiation output detected with a suitable variety of THz filters and μWv detectors. Shown in Fig. 3(b) are two pressure scans of the μWv output Φ of laser plasmas driven in air by 35-fs laser pulses with pulse energies of $\approx$10 mJ and $\approx$60 mJ. In agreement with expectations based on our modeling [Figs. 1(a)–1(c)], the pressure scan for the μWv output driven by 10-mJ laser pulses is strikingly different from the $\Phi(p)$ scan in experiments with a 60-mJ laser driver.
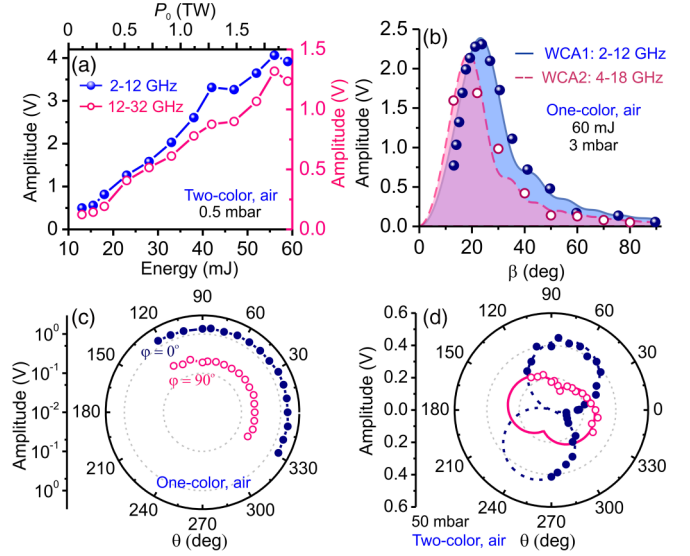
The $\Phi(p)$ scan measured with a 10-mJ driver displays, as expected, deviations from a monotonic behavior, featuring plateaus, centered at around $p_1 \approx 0.1$ bar and $p_2 \approx 3$ mbar [filled circles in Fig. 3(b)]. The $\Phi(p)$ scan measured with a 60-mJ driver, on the other hand, is uniformly monotonic [open circles in Fig. 3(b)], suggesting that laser-driven ionization of N_2 is dominated by multiple ionization within the entire range of gas pressures covered by this scan. The electron density that multiple ionization provides is high enough to defocus the plasma beam, via the transverse profile of $\delta n_{\rm p}$, thus limiting the field intensity in the focusing laser beam. A similar behavior is observed for pressure scans measured with a 60-mJ laser driver for other molecular (air and N_2) and atomic (argon) gases [Fig. 3(c)], as well as in experiments with a two-color driver [Fig. 3(d)].

C. Spatial mode structure

The spatial mode profiles of microwave fields emitted from laser-driven plasmas are analyzed by scanning the WCA detector in the β angle (Fig. 2) and measuring the microwave output as a function of β with the distance D between the WCA and the plasma source fixed at $D \approx 20$ cm. As one of the central results of these studies, the low-p enhancement

of microwave generation, typical of a high-P_0 regime of laser-plasma interactions [Figs. 3(b)–3(d)], is found to correlate with a buildup of coherence, as indicated by a well-resolved emission cone that shows up in the spatial mode profile of microwave radiation from low-p laser plasmas.

To gain physical insights into these findings, we resort to the physical picture of low-frequency secondary radiation emission by transient plasma currents induced in a gas in the wake of a laser-driven ionization front [5–7]. The electrons that constitute such currents move at speeds well below the speed of light. The laser-induced ionization front that drives these currents, however, propagates through the gas along with the laser pulse. The speed of this ionization front can be close to or even higher than the phase velocity of THz/microwave radiation, giving rise to THz/microwave radiation patterns [5–7] in the form of a Cherenkov emission cone [33,34,49,50].

In Fig. 4(b), we present typical $\mathcal{F}(\beta)$ scans of the μWv field measured in two frequency ranges with a single-color 0.8-μm, 35-fs, 60-mJ laser driver focused in air at $p \approx 3$ mbar. These $\mathcal{F}(\beta)$ scans are seen to display well-resolved peaks indicating a buildup of spatial coherence in the μWv field. Also shown in Fig. 4(b) are the phase-matching functions of Cherenkov radiation [5–7], $\mathcal{I}(\beta) = \int_{\omega_1}^{\omega_2} S(\omega) \sin^2 \beta \sin^2[(\omega/c)L \sin^2(\beta/2)][\sin(\beta/2)]^{-4} d\omega$, where $S(\omega)$ is the radiation spectrum and L is the plasma channel length.

With ω_1 and ω_2, as dictated by the respective WCA detection ranges in these experiments, $\omega_1 \approx 4.7$ GHz and $\omega_2 \approx 8.2$ GHz for WCA1 and $\omega_1 \approx 7.8$ GHz and $\omega_2 \approx 12$ GHz for WCA2, $\mathcal{I}(\beta)$ fits are seen to agree very well with experimental $\mathcal{F}(\beta)$ profiles of the μWv output [cf. experimental data points and the results of simulations in Fig. 4(b)]. At higher gas pressures, no evidence of coherence buildup is observed in β scans of the microwave output. This result is consistent with the pressure scans in Fig. 3(b), showing a drastic decrease in the microwave output at high gas pressures, as well as with the results of numerical modeling. Moreover, these findings are consistent with the earlier studies by Englesbe *et al.* [16], reporting no or little evidence of coherence buildup in the microwave output of midinfrared-driven laser plasmas at high gas pressures.

In a canonical picture of nonlinear-optical interactions with a well-controlled number of emitters N, a coherent signal buildup implies a signature N^2 scaling of the nonlinear signal. In the laser-plasma setting, however, N is no longer an independent variable that can be changed at will, e.g., by varying the gas pressure. Indeed, an equivalent of N can be brought to a picture of microwave generation by plasma currents via the electron density, $N = \rho$, and a straightforward equation $j_z = e\rho u_z$, u_z being the z component of the electron velocity. The electron density, however, cannot be varied by simply changing the gas pressure or any other externally controllable parameter. Instead, the electron density builds up as a part of laser-driven ionization dynamics [Eq. (2)] that plays out self-consistently with a spatiotemporal evolution of the laser field [Eq. (1)]. In such a setting, the buildup of ρ is coupled to an intricate space-time field dynamics, accompanied by changes in the field intensity, thus giving rise to a complex,

non-N^2 behavior of the nonlinear signal as a function of the gas pressure.

D. Polarization-resolved studies

1. Single-color experiments

In Fig. 4(c), we present the results of polarization-resolved studies of microwave radiation emitted from laser plasmas driven in air at $p \approx 1$ mbar by a single-color 0.8-μm, 35-fs, 60-mJ laser driver. The microwave output Φ of laser plasmas is measured in these experiments with the coaxial cable of the WCA2 detector first set at $\varphi = 0$ [filled blue circles in Fig. 4(c)] and then at $\varphi = \pi/2$ (open pink circles). With the WCA set at $\varphi = 0$, a pure radially polarized mode would show up as a perfect circle in the polar plot of Φ as a function of θ, $\Phi = $ const. A linearly polarized radiation mode, on the other hand, would have manifested itself in this setting as a signature $\sin^2\theta$, figure-of-eight $\Phi(\theta)$ polar trace. As can be seen from Fig. 4(c), a $\Phi = $ const, circular plot [blue solid line in Fig. 3(c)] fits the $\Phi(\theta)$ measurements [filled circles in Fig. 3(c)] remarkably well, with a standard deviation within 4%. No sign of a figure-of-eight θ dependence that would be indicative of a linearly polarized mode is observed in the measured $\Phi(\theta)$.

With the WCA set at $\varphi = \pi/2$, a pure radially polarized mode does not contribute to the WCA readout. The WCA signal in this setting is more than an order of magnitude weaker than the WCA signal in the $\varphi = 0$ arrangement. With the signal from the radially polarized radiation mode completely suppressed, the $\varphi = \pi/2$ detection setting provides a much more sensitive probe for linearly polarization radiation. Remarkably, even in this setting, the $\Phi(\theta)$ trace shows no signs of θ dependence.

Polarization-resolved measurements thus show that microwave radiation generated in single-color laser-plasma experiments is dominated by a radially polarized mode (double-headed arrows in Fig. 2). This finding indicates the dominant role of ponderomotively driven longitudinal plasma currents as a source of microwave radiation. That the WCA detector set at $\varphi = \pi/2$ yields an order of magnitude weaker, yet nonvanishing, θ-independent readout [pink circles and solid line in Fig. 4(c)] suggests the existence of an incoherent component of microwave radiation, which may be indicative, as one possibility, of incoherent bremsstrahlung from laser-driven plasmas [51].

2. Two-color experiments

Microwave radiation with drastically different polarization properties is observed in experiments with a two-color driver [Fig. 4(d)]. In these experiments, the 0.8-μm, 35-fs, 60-mJ amplified TiS-laser output is mixed with its $\phi_{SH} = \pi/2$ phase-shifted second harmonic with a central wavelength at $\lambda_{SH} = \lambda_0/2$ and a variable pulse energy E_{SH} to yield a field with broken time symmetry [3]. Both the 0.8-μm field and its second harmonic are linearly polarized in our experimental setting, as verified by careful polarization measurements.

Unlike a single-color driver, such a two-color field induces transverse photoionization currents that do not cancel within the field cycle [3]. The symmetry of such currents dictates

emission of linearly polarized radiation fields. In agreement with these symmetry arguments, polarization analysis of microwave radiation in our two-color laser-plasma experiments yields polar plots [open and filled circles in Fig. 4(d)] that closely follow $\sin^2(\varphi + \varphi_0)$ fits [respective solid and dotted lines in Fig. 4(d)]. With the WCA probe rotated by $\pi/2$, the polar plot of the microwave field is seen to also rotate by the same angle [cf. open and filled circles in Fig. 4(d)], exactly as dictated by the geometry of our polarization analysis. Results of these experiments indicate, in agreement with an extensive literature on two-color THz generation [3,8,18,28–30], the dominant role of transverse currents as sources of THz radiation.

E. Microwave radiation by plasma currents

To gain deeper insights into the physics behind microwave generation and to understand the spectral properties of microwave radiation in our experiments, we consider the longitudinal plasma current [5,6] that provides a source term in the frequency-domain field evolution equation for an ultrashort laser driver:

$$j_z(r, z, \omega) = \frac{e\omega\omega_p^2(r,z)(\omega + 2i\nu_e)}{2mc^2\omega_0^2(\omega^2 - \omega_p^2(r,z) + i\nu_e\omega)}$$
$$\times \int_{-\infty}^{\infty} A(r, z, \omega')A^*(r, z, \omega - \omega')d\omega', \quad (3)$$

$$j_z(r, z, \omega) = \frac{e\omega\omega_p^2(r,z)(\omega + 2i\nu_e)}{2mc^2\omega_0^2(\omega^2 - \omega_p^2(r,z) + i\nu_e\omega)}$$
$$\times \int_{-\infty}^{\infty} I(r, z, \eta)e^{-i\omega\eta}d\eta, \quad (4)$$

where $\omega_p(r,z) = \omega_p(r, z, \eta > \tau_0)$ is the plasma frequency in the wake of the laser pulse.

At each point (r, z) within the laser plasma, the current j_z emits radiation with intensity spectrum, $S(r, z, \omega) \propto |j_z(r, z, \omega)|^2$, that peaks at around $\omega_p(r, z)$, falls off as $I(r, z, \omega)$ in its high-frequency tail, and scales as ω^2 in the low-frequency limit, i.e., for $\omega \ll \omega_p, \nu_e, 1/\tau_0$. In Fig. 5(a), we plot a map of the electron density $\rho(r, z) = \rho(r, z, \eta > \tau_0)$ found by solving the field evolution Eq. (1) jointly with Eq. (2) for $\rho(r, z, \eta)$. Also shown in Fig. 5(a) are the contour lines, dividing this map into eight areas, with the electron density $\rho(r, z)$ and, hence, the plasma frequency $\omega_p(r, z)$ increasing from the outermost area (area 1) to the innermost, central region of the laser plasma (area 8).

Figure 5(b) presents radiation spectra $S_q(\omega) \propto |\int_{V_q} j_z(r, z, \omega)2\pi r dr dz|^2$, calculated by integrating over the volume V_q of the qth plasma region, with q taking the values from 1 to 8, enumerating the plasma regions as shown in Fig. 5(a). Because the electron density $\rho(r, z)$ decreases from the central region the laser plasma to its outer areas.

Because the electron density $\rho(r, z)$ is highest within plasma region 8, plasma currents j_z induced in this region emit radiation with the highest frequencies. The spectrum of this radiation, $S_8(\omega)$, peaks at around 10 THz [curve 8 in Fig. 5(b)]. However, most of this radiation never makes it out of the laser plasma as it is strongly attenuated by
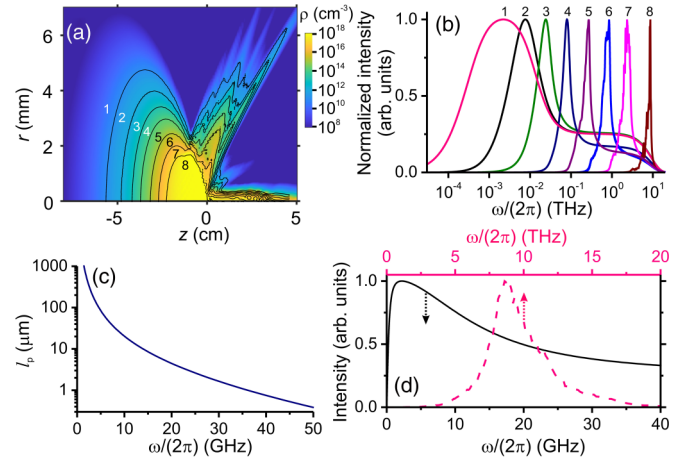

FIG. 5. (a) A map of the electron density $\rho(r, z) = \rho(r, z, \eta > \tau_0)$ found by solving the field evolution Eq. (1) jointly with Eq. (2) for a laser pulse with $\lambda_0 = 0.8\,\mu m$, $\tau_0 = 35\,fs$, $d_0 = 7\,cm$, $P_0 = 1.5\,TW$, and $f = 2.5\,m$ in a gas cell filled with argon at $p = 0.1\,bar$. Also shown are the contour lines, dividing the map into eight areas, with the electron density below $10^{11}\,cm^{-3}$ (1) and ranging from 10^{11} to $10^{12}\,cm^{-3}$ (2), 10^{12} to $10^{13}\,cm^{-3}$ (3), 10^{13} to $10^{14}\,cm^{-3}$ (4), 10^{14} to $10^{15}\,cm^{-3}$ (5), 10^{15} to $10^{16}\,cm^{-3}$ (6), 10^{16} to $10^{17}\,cm^{-3}$ (7), and 10^{17} to $10^{18}\,cm^{-3}$ (8). (b) Radiation spectra calculated by integrating over the volume V_q of the qth plasma region, with $q = 1$ (curve 1), 2 (2), 3 (3), 4 (5), 5 (5), 6 (6), 7 (7), and 8 (8). (c) Plasma attenuation length l_p as a function of radiation frequency for a plasma with an electron density of $10^{11}\,cm^{-3}$ and the electron collision rate $\nu_e = 0.3\,THz$. (d) Radiation spectra calculated by integrating over the total volume of plasma regions 1–8 (dashed pink line) and the volume V_1 of the subsurface plasma region with $q = 1$ (solid black line).

plasma screening within a typical attenuation length $l_p = c(2\omega)^{-1}\,Im\,[(\omega^2 + i\nu_e\omega)^{1/2}\,(\omega^2 + i\nu_e\omega - \omega_p^2)^{-1/2}]$ [Fig. 5(c)]. Because of this screening effect, the radiation flux that does couple out of the laser plasma and reach the detectors is dominated by emission from outer plasma regions. Since $\rho(r, z)$ in these regions is much lower than the electron density that the driver pulse leaves behind within the innermost plasma areas, the spectrum of radiation that overcomes plasma screening is shifted toward lower frequencies relative to radiation generated in the central regions of the laser plasma [Figs. 5(b) and 5(d)]. Specifically, the spectra of radiation emitted from the subsurface plasma areas [regions 1 and 2 in Fig. 5(a)] peak, respectively, at around 2.0 and 7.5 GHz [curves 1 and 2 in Fig. 5(b)]. This analysis is consistent with bright microwave radiation detected by all the WCA detectors in our laser-plasma experiments. Moreover, the physical picture of microwave supercontinuum generation distributed over the plasma volume, with different subbands of microwave supercontinua emitted from different plasma regions, is overall consistent with the difference in the pressure dependence of radiation intensity within different subbands of microwave supercontinua observed in experimental pressure scans [Fig. 3(d)]. While these experimental data can in no way conclusively confirm this physical picture, they are reasonably explained in terms of spatially nonuniform, pressure-dependent electron density distribution and plasma

attenuation of broadband microwave radiation emitted from different regions in the volume of laser-driven plasmas.

V. CONCLUSION

To summarize, ultrafast laser-plasma interactions driven by TW laser pulses give rise to a bright multioctave microwave radiation, whose polarization and spatial mode structure provides a sensitive probe for laser-driven plasma electrodynamics, helping detect the symmetries of plasma currents and signatures of multiple ionization. Polarization mode structure of this radiation is dominated by a radially polarized mode, indicating the significance of ponderomotively driven plasma currents as sources of microwave emission. Angle-resolved studies reveal regimes in which microwave emission is drastically enhanced, via coherence buildup, manifested in a well-resolved Cherenkov-emission cone.

[1] D. J. Cook and R. M. Hochstrasser, Opt. Lett. **25**, 1210 (2000).

[2] X. Xie, J. Dai, and X.-C. Zhang, Phys. Rev. Lett. **96**, 075005 (2006).

[3] K. Y. Kim, A. J. Taylor, J. H. Glownia, and G. Rodriguez, Nat. Photonics **2**, 605 (2008).

[4] C. D'Amico, A. Houard, M. Franco, B. Prade, A. Mysyrowicz, A. Couairon, and V. T. Tikhonchuk, Phys. Rev. Lett. **98**, 235002 (2007).

[5] P. Sprangle, J. Peñano, B. Hafizi, and C. Kapetanakos, Phys. Rev. E **69**, 066415 (2004).

[6] I. Thiele, R. Nuter, B. Bousquet, V. Tikhonchuk, S. Skupin, X. Davoine, L. Gremillet, and L. Bergé, Phys. Rev. E **94**, 063202 (2016).

[7] C. D'Amico, A. Houard, S. Akturk, Y. Liu, M. Franco, B. Prade, A. Couairon, V. Tikhonchuk, and A. Mysyrowicz, New J. Phys. **10**, 013015 (2007).

[8] I. Babushkin, W. Kuehn, C. Köhler, S. Skupin, L. Bergé, K. Reimann, M. Woerner, J. Herrmann, and T. Elsaesser, Phys. Rev. Lett. **105**, 053903 (2010).

[9] T. Balciunas, A. J. Verhoef, A. V. Mitrofanov, G. Fan, E. E. Serebryannikov, M. Y. Ivanov, A. M. Zheltikov, and A. Baltuska, Chem. Phys. **414**, 92 (2013).

[10] N. Horiuchi, Nat. Photonics **4**, 140 (2010).

[11] S. Tzortzakis, G. Méchain, G. Patalano, Y.-B. André, B. Prade, M. Franco, A. Mysyrowicz, J.-M. Munier, M. Gheudin, G. Beaudin, and P. Encrenaz, Opt. Lett. **27**, 1944 (2002).

[12] C. D'Amico, A. Houard, M. Pellet, Ch Pichot, and A. Mysyrowicz, J. Phys. D: Appl. Phys. **41**, 245206 (2008).

[13] Y. Brelet, A. Houard, G. Point, B. Prade, J. Carbonnel, Y.-B. Andre, M. Pellet, and A. Mysyrowicz, Appl. Phys. Lett. **101**, 264106 (2012).

[14] B. Forestier, A. Houard, M. Durand, Y.-B. André, B. Prade, J.-Y. Dauvignac, F. Perret, C. Pichot, M. Pellet, and A. Mysyrowicz, Appl. Phys. Lett. **96**, 141111 (2010).

[15] F. Théberge, J.-F. Gravel, J.-C. Kieffer, F. Vidal, and M. Châteauneuf, Appl. Phys. Lett. **111**, 073501 (2017).

[16] A. Englesbe, J. Elle, R. Reid, A. Lucero, H. Pohle, M. Domonkos, K. Krushelnick, and A. Schmitt-Sody, Opt. Lett. **43**, 4953 (2018).

[17] T. I. Oh, Y. S. You, N. Jhajj, E. W. Rosenthal, H. M. Milchberg, and K. Y. Kim, New J. Phys. **15**, 075002 (2013).

[18] A. D. Koulouklidis, V. Shumakova, C. Gollner, V. Yu. Fedorov, A. Pugžlys, A. Baltuška, and S. Tzortzakis, Nat. Commun. **11**, 292 (2020).

[19] A. V. Mitrofanov, D. A. Sidorov-Biryukov, M. M. Nazarov, A. A. Voronin, M. V. Rozhko, A. D. Shutov, S. V. Ryabchuk, E. E. Serebryannikov, A. B. Fedotov, and A. M. Zheltikov, Optica **7**, 15 (2020).

[20] A. A. Voronin and A. M. Zheltikov, Phys. Rev. A **101**, 043813 (2020).

[21] M. Schultze, E. M. Bothschafter, A. Sommer, S. Holzner, W. Schweinberger, M. Fieß, M. Hofstetter, R. Kienberger, V. Apalkov, V. S. Yakovlev, M. I. Stockman, and F. Krausz, Nature (London) **493**, 75 (2012).

[22] M. Garg, M. Zhan, T. T. Luu, H. Lakhotia, T. Klostermann, A. Guggenmos, and E. Goulielmakis, Nature (London) **538**, 359 (2016).

[23] G. Vampa, T. J. Hammond, M. Taucer, X. Ding, X. Ropagnol, T. Ozaki, S. Delprat, M. Chaker, N. Thiré, B. Schmidt, F. Légaré, D. Klug, A. Naumov, D. Villeneuve, A. Staudte, and P. Corkum, Nat. Photonics **12**, 465 (2018).

[24] E. A. Nanni, W. R. Huang, K.-H. Hong, K. Ravi, A. Fallahi, G. Moriena, R. J. Dwayne Miller, and F. X. Kärtner, Nat. Commun. **6**, 8486 (2015).

[25] T. Kampfrath, A. Sell, G. Klatt, A. Pashkin, S. Mährlein, T. Dekorsy, M. Wolf, M. Fiebig, A. Leitenstorfer, and R. Huber, Nat. Photonics **5**, 31 (2011).

[26] F. Langer, C. P. Schmid, S. Schlauderer, M. Gmitra, J. Fabian, P. Nagler, C. Schüller, T. Korn, P. G. Hawkins, J. T. Steiner, U. Huttner, S. W. Koch, M. Kira, and R. Huber, Nature (London) **557**, 76 (2018).

[27] A. A. Lanin, E. A. Stepanov, A. B. Fedotov, and M. A. Zheltikov, Optica **4**, 516 (2017).

[28] L. Bergé, S. Skupin, C. Köhler, I. Babushkin, and J. Herrmann, Phys. Rev. Lett. **110**, 073901 (2013).

[29] Y. S. You, T. I. Oh, and K. Y. Kim, Phys. Rev. Lett. **109**, 183902 (2012).

[30] I. Thiele, B. Zhou, A. Nguyen, E. Smetanina, R. Nuter, K. J. Kaltenecker, P. González de Alaiza Martínez, J. Déchard, L. Bergé, P. U. Jepsen, and S. Skupin, Optica **5**, 1617 (2018).

[31] C. D'Amico, A. Houard, M. Franco, B. Prade, and A. Mysyrowicz, Opt. Express **15**, 15274 (2007).

[32] A. Englesbe, R. Schwartz, A. Korolov, D. Jang, D. Woodbury, K. Kim, H. Milchberg, R. Reid, A. Lucero, H. Pohle, S. Kalmykov, K. Krushelnick, A. Schmitt-Sody, and J. Elle, Microwave Radiation from Single and Two Color Mid-Infrared Laser Produced Plasmas in Air, in *Conference on Lasers and Electro-Optics*, OSA Technical Digest (Optical Society of America, Washington, DC, 2019), paper FTh1M.3.

[33] I. Frank and I. Tamm, Dokl. Akad. Sci. URSS **14**, 109 (1937).

[34] I. Tamm, J. Phys. USSR **1**, 439 (1939).

[35] L. Bergé, S. Skupin, R. Nuter, J. Kasparian, and J.-P. Wolf, Rep. Prog. Phys. **70**, 1633 (2007).

[36] A. A. Voronin and A. M. Zheltikov, Phys. Rev. A **94**, 023824 (2016).

[37] A. A. Voronin and A. M. Zheltikov, Phys.-Usp. **59**, 869 (2016).

[38] P. B. Glek, A. A. Voronin, V. Ya. Panchenko, and A. M. Zheltikov, Laser Phys. Lett. **17**, 055401 (2020).

[39] A. Börzsönyi, Z. Heiner, M. P. Kalashnikov, A. P. Kovács, and K. Osvay, Appl. Opt. **47**, 4856 (2008).

[40] E. R. Peck and D. J. Fisher, J. Opt. Soc. Am. **54**, 1362 (1964).

[41] A. Couairon and A. Mysyrowicz, Phys. Rep. **441**, 47 (2007).

[42] L. V. Keldysh, Zh. Eksp. Teor. Fiz. **47**, 1945 (1964) [Sov. Phys. JETP **20**, 1307 (1965)].

[43] A. E. Kramida, Yu. Ralchenko, and J. Reader, and NIST ASD Team, NIST Atomic Spectra Database (version 5.8) (2021). Available online at: https://physics.nist.gov/asd.

[44] P. A. Zhokhov, V. Ya. Panchenko, and A. M. Zheltikov, Phys. Rev. A **86**, 013835 (2012).

[45] A. V. Mitrofanov, M. M. Nazarov, A. A. Voronin, D. A. Sidorov-Biryukov, V. Ya. Panchenko, and A. M. Zheltikov, Opt. Lett. **43**, 5693 (2018).

[46] M. M. Nazarov, A. V. Mitrofanov, D. A. Sidorov-Biryukov, M. V. Chaschin, P. A. Shcheglov, A. M. Zheltikov, and V. Ya. Panchenko, Infrared J. Millimeter Terahertz Waves **41**, 1069 (2020).

[47] G. A. Mourou, T. Tajima, and S. V. Bulanov, Rev. Mod. Phys. **78**, 309 (2006).

[48] S.-Y. Chen, G. S. Sarkisov, A. Maksimchuk, R. Wagner, and D. Umstadter, Phys. Rev. Lett. **80**, 2610 (1998).

[49] P. A. Cherenkov, Phys. Rev. **52**, 378 (1937).

[50] L. D. Landau, E. M. Lifshitz, and L. P. Pitaevskii, *Electrodynamics of Continuous Media*, 2nd ed. (Butterworth–Heinemann, Oxford, 1984).

[51] W. Hoyer, A. Knorr, J. V. Moloney, E. M. Wright, M. Kira, and S. W. Koch, Phys. Rev. Lett. **94**, 115004 (2005).